Structure and Properties of Nano-Scale Oxide-Dispersed Iron

R. VIJAY, M. NAGINI, S.S. SARMA, M. RAMAKRISHNA, A.V. REDDY, and G. SUNDARARAJAN

Bulk samples of pure iron and yttria dispersed iron with and without titanium (*i.e.*, Fe, Fe-Y_2O_3, and Fe-Y_2O_3-Ti) were prepared by hot extrusion of high-energy ball-milled powders. An examination of the microstructure using TEM revealed that the addition of titanium resulted in the reduction of the dispersoid size with a concomitant increase in the volume fraction of the dispersoids. As a result, Fe-Y_2O_3-Ti exhibited a substantial increase in hardness and tensile properties as compared to Fe and Fe-Y_2O_3. The higher hardness and strength of Fe-Y_2O_3-Ti is shown to be due to the presence of finer and higher number density of Y-Ti-O complex oxides. Dynamic strain aging in the temperature range of 423 K to 573 K (150 °C to 300 °C) was observed in all the compositions studied.

DOI: 10.1007/s11661-013-2019-x

I. INTRODUCTION

DISPERSION of fine oxide particles in a metal matrix is a well-known strengthening mechanism that has led to the development of alloys with outstanding strength and creep resistance. In the recent past, a few Fe-Cr steels containing dispersion of nano-scale oxides based on Y-Ti-O have been developed.[1–5] The thermal stability of the complex oxides coupled with the oxide induced microstructural stability makes the oxide dispersion strengthened (ODS) steels ideal candidate materials for applications involving prolonged exposure to high temperatures. The ODS steels exhibit excellent resistance to irradiation damage and swelling and hence hold promise for use as clad and structural materials in nuclear reactors.[6,7]

ODS materials are produced either by internal oxidation or by powder metallurgical techniques. The popular powder metallurgical processing involves mechanical alloying (MA) and powder consolidation by hot isostatic pressing and/or hot working. ODS steels containing Y_2O_3 are produced by MA, resulting in the formation of fine oxide particles. The mechanism of nano-sclae (10 to 20 nm) Y_2O_3 particle formation is not yet clearly understood. While one group advocates that the oxide particle size reduces due to fragmentation during MA,[8–10] another group strongly supports the idea that Y_2O_3 fragments, dissociates and dissolves in the matrix during milling and precipitates as nano-sized particles during the hot consolidation stage.[11–16] However, all the investigations have clearly established that the presence of Ti in the steel results in the formation of Y-Ti-O based complex oxides in the size range 3 to 8 nm instead of much coarser Y_2O_3.[8–18]

The studies so far conducted on ODS ferrous materials are focussed on Cr-containing steels with Y_2O_3 or Y-Ti-O as the dispersoids. No systematic study has been carried out to assess the role of Y_2O_3 and Y-Ti-O dispersoids in pure iron except for the recent study carried out by the present authors.[19] The present study, an extension of the earlier work,[19] has been undertaken to examine the influence of fine Y_2O_3 and Y-Ti-O dispersoids in hot extruded bulk iron samples without the influence of alloying elements like C and Cr on mechanical properties.

II. EXPERIMENTAL

Pure iron, Fe-0.35 wt pct Y_2O_3, and Fe-0.2 wt pct Ti-0.35 wt pct Y_2O_3 compositions were produced by MA using Fe, Y_2O_3, and Ti powders, details of which are given in Table I. Large (1 kg) batches of Fe, Fe-0.35Y_2O_3, and Fe-0.35Y_2O_3-0.2Ti compositions were prepared by milling elemental powders in an attritor at 300 rpm for 40 hours. Hardened steel balls of 6 mm diameter were used for milling in an austenitic steel container and a ball to powder ratio of 15:1 was maintained. The milled powder was filled in mild steel cans of 46 mm ϕ, 75 mm height, degassed at 723 K (450 °C) and sealed. The sealed cans were upset at 1323 K (1050 °C) under a pressure of 125 MPa and the upset cans were extruded at 1323 K (1050 °C) under 160 MPa to 16 mm ϕ rods with an extrusion ratio of 9. The extruded rods were annealed at 1223 K (950 °C) for 0.5 hour and then air cooled to room temperature. The O, N, C, and S analysis of milled powders was carried out using oxygen/nitrogen (LECO, Model: TC436) and carbon/sulfur (LECO, Model: CS444) analysers. Atomic emission spectroscopy was used to estimate Cr, Ti, and Y content. Microstructural examination of extruded and annealed bulk samples was carried out using SEM (Hitachi, S-4300SE/N). Samples were etched using 2 pct nital for microstructural observations. Grain size was estimated by intercept method and the number of grains

R. VIJAY, Scientist "E", M. NAGINI, SAF, S.S. SARMA and M. RAMAKRISHNA, Scientists "C", A.V. REDDY, Consultant, and G. SUNDARARAJAN, Director, are with the International Advanced Research Centre for Powder Metallurgy & New Materials (ARCI), Balapur, Hyderabad 500 005, India. Contact e-mail: director@arci.res.in
Manuscript submitted June 3, 2013.
Article published online October 2, 2013

Table I. Details of the Powders Used

Name	Purity (Pct)	O (Wt Pct)	N (Wt Pct)	Avg. Particle Size	Source
Iron Powder	99.5	0.2	0.018	150 μm	SFL, India
Titanium Powder	99.8	0.1	0.02	105 μm	Crucible Research, USA
Y_2O_3 Powder	99.95	21.3	—	40 nm	Inframat Advanced Materials, USA

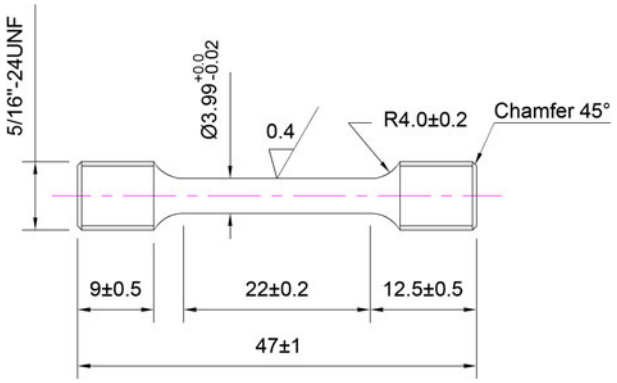

Fig. 1—Drawing of tensile specimen.

measured was in the range 1200 to 1500 for each composition, *i.e.*, Fe, Fe-Y_2O_3, and Fe-Ti-Y_2O_3.

Transmission electron microscopic (TEM) investigations were carried out using a FEI Tecnai G20 200kV (LaB_6) microscope equipped with Gatan image filter capable of carrying out imaging and electron energy loss spectroscopy. The EDS spectra were collected using an EDAX silicon thin window detector. Samples were sectioned from annealed rods and subsequently ground, polished, dimpled, and ion-milled as per standard procedure. The dispersoid sizes were estimated using image analysis software. About 2500 dispersoids spread over 7 TEM images were measured for their size for each of the two compositions, *i.e.*, Fe-Y_2O_3 and Fe-Y_2O_3-Ti alloys. Once the frequency distribution of the dispersoid diameter was obtained for each composition, the corresponding volume fraction of dispersoids (f) was estimated using the Eq. [1] given below.[20]

$$f = \frac{\pi \sum N_i d_i^3}{6At} \quad [1]$$

In Eq. [1], N_i is the number of dispersoids having a diameter of d_i, A is the total projection area, and t is the foil thickness. The foil thickness was measured using convergent beam electron diffraction (CBED) pattern.

Hardness of the annealed rods was measured at 5 kgf load using Vickers macro hardness testing machine (LECO, Model: LV-700AT) under standard test conditions. The tensile properties of the annealed rods were evaluated from room temperature to 723 K (450 °C) at a strain rate of 7.5×10^{-4} s^{-1} using universal testing machine (Make: INSTRON, Model No: 4507), having a capacity of 200 KN with a furnace to heat the sample up to 1273 K (1000 °C). The tensile test specimen geometry is given in Figure 1.

III. RESULTS AND DISCUSSION

A. *Chemical Composition*

The chemical composition of the Fe, Fe-Y_2O_3, and Fe-Y_2O_3-Ti annealed rods is given in Table II. Comparison of the compositions of the raw materials used and the processed bars indicated that chromium was picked up during milling from the milling vial and media. Oxygen and nitrogen enrichment was also observed due to minor leakages during milling.

B. *Microstructure*

Microstructure and mechanical properties of identically processed Fe, Fe-Y_2O_3, and Fe-Y_2O_3-Ti extruded rods were evaluated after annealing. The microstructures of all the three compositions are shown in Figures 2(a) through (c). The structure consisted of equi-axed grains of ferrite. A few coarse oxide particles were observed in the ODS iron samples. The grain size distribution in all the three compositions is given in Figures 3(a) through (c). The average grain intercepts for Fe, Fe-Y_2O_3, and Fe-Y_2O_3-Ti were 14, 11, and 8 μm respectively. Though there is no substantial difference in the grain size between Fe and Fe-Y_2O_3, significant grain refinement is evident in Fe-Y_2O_3-Ti. The influence of the oxide dispersoids in pinning the grain boundaries and inhibiting grain growth, in spite of repeated exposure to high temperatures during processing, is well known. As will be shown later, the refinement of grain size in Fe-Y_2O_3-Ti is the result of the grain boundary pinning effects of fine (12 nm) Y-Ti-O complex dispersoids. The relative ineffectiveness of the dispersoids in grain refinement in Fe-Y_2O_3 sample can be attributed to the much coarser (20 nm) Y_2O_3 dispersoids.

TEM examination was carried out on ODS iron rods to examine the size and volume fraction of dispersoids. The oxide particles and corresponding EDS patterns for Fe-Y_2O_3 and Fe-Y_2O_3-Ti are shown in Figures 4(a) through (d), respectively. The distribution of dispersoids in ODS irons are shown in Figure 5. The results indicate that the dispersoids in Fe-Y_2O_3 samples are Y_2O_3 with an average size of 20.5 nm, whereas in Fe-Y_2O_3-Ti samples, the average size of dispersoids is 12 nm and are oxide complexes consisting of Y-Ti-O. The number density of dispersoids in Fe-Y_2O_3 and Fe-Y_2O_3-Ti are 7.0×10^{21} and 3.9×10^{22} per cubic meter, respectively. Using the experimentally obtained dispersoid diameter and number density, the volume fraction (f) has been calculated as 0.327 pct and 1.04 pct in the case of Fe-Y_2O_3 and Fe-Y_2O_3-Ti (see Table IV). On considerations of the atomic ratio of yttrium to titanium, which in the experimental sample is 0.6, it can be concluded

Table II. Chemical Composition (Wt Pct) of the Annealed Rods

Material	C	O	N	Cr	Ti	Y_2O_3	Fe
Fe	0.028	0.44	0.018	0.019	—	—	balance
Fe-Y_2O_3	0.028	0.51	0.019	0.018	—	0.30	balance
Fe-Y_2O_3-Ti	0.027	0.47	0.018	0.019	0.19	0.28	balance

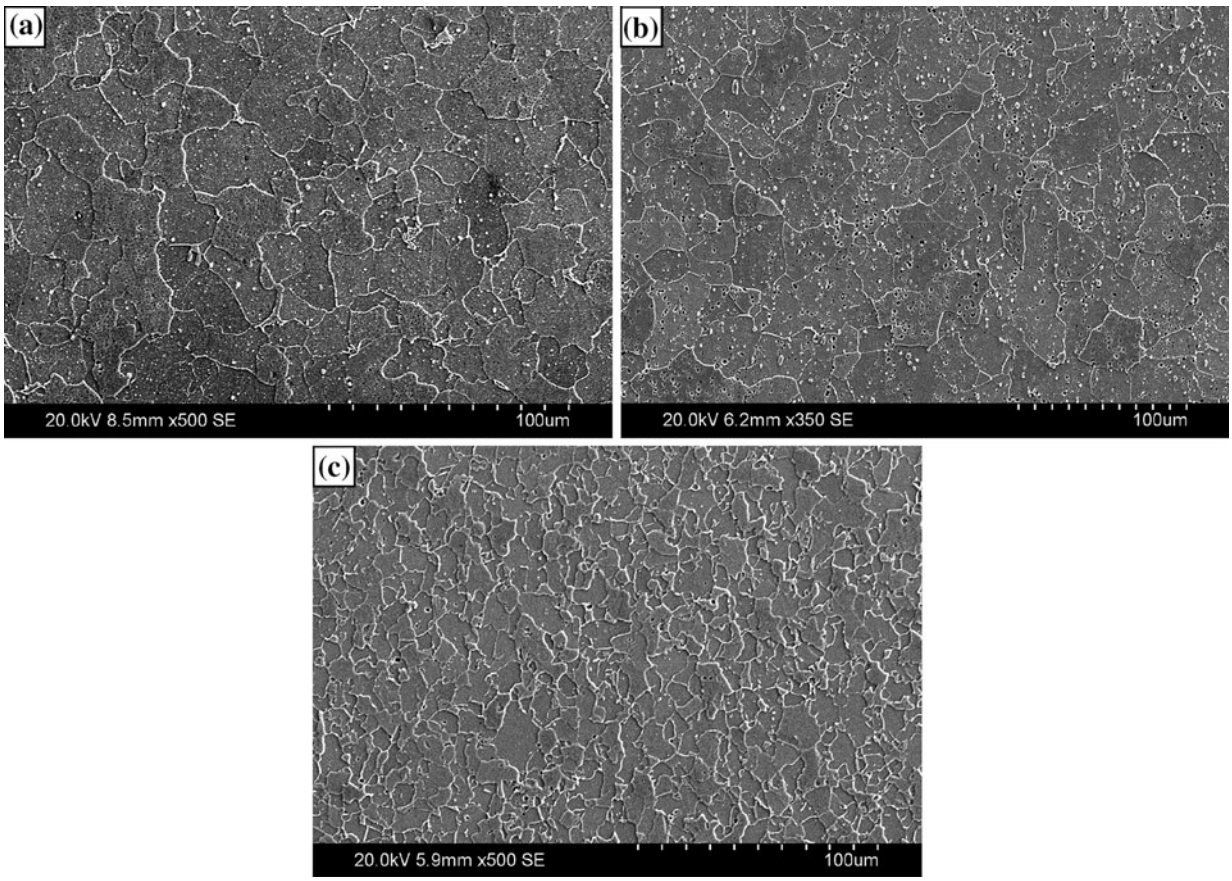

Fig. 2—Microstructures of extruded and annealed rods in longitudinal direction: (*a*) Fe, (*b*) Fe-Y_2O_3, and (*c*) Fe-Y_2O_3-Ti.

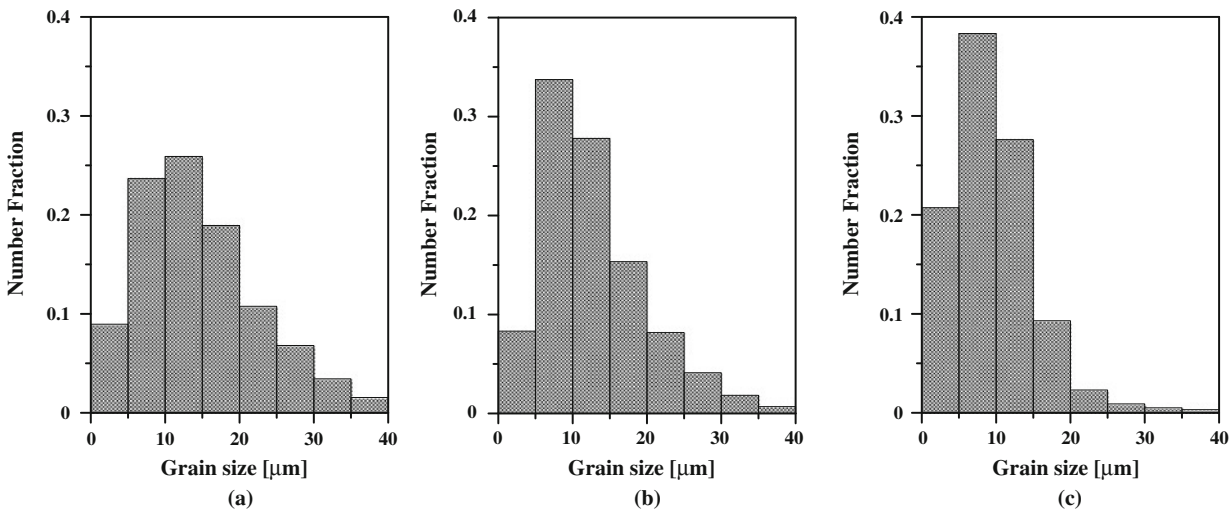

Fig. 3—Grain size distribution in extruded and annealed rods: (*a*) Fe, (*b*) Fe-Y_2O_3, and (*c*) Fe-Y_2O_3-Ti.

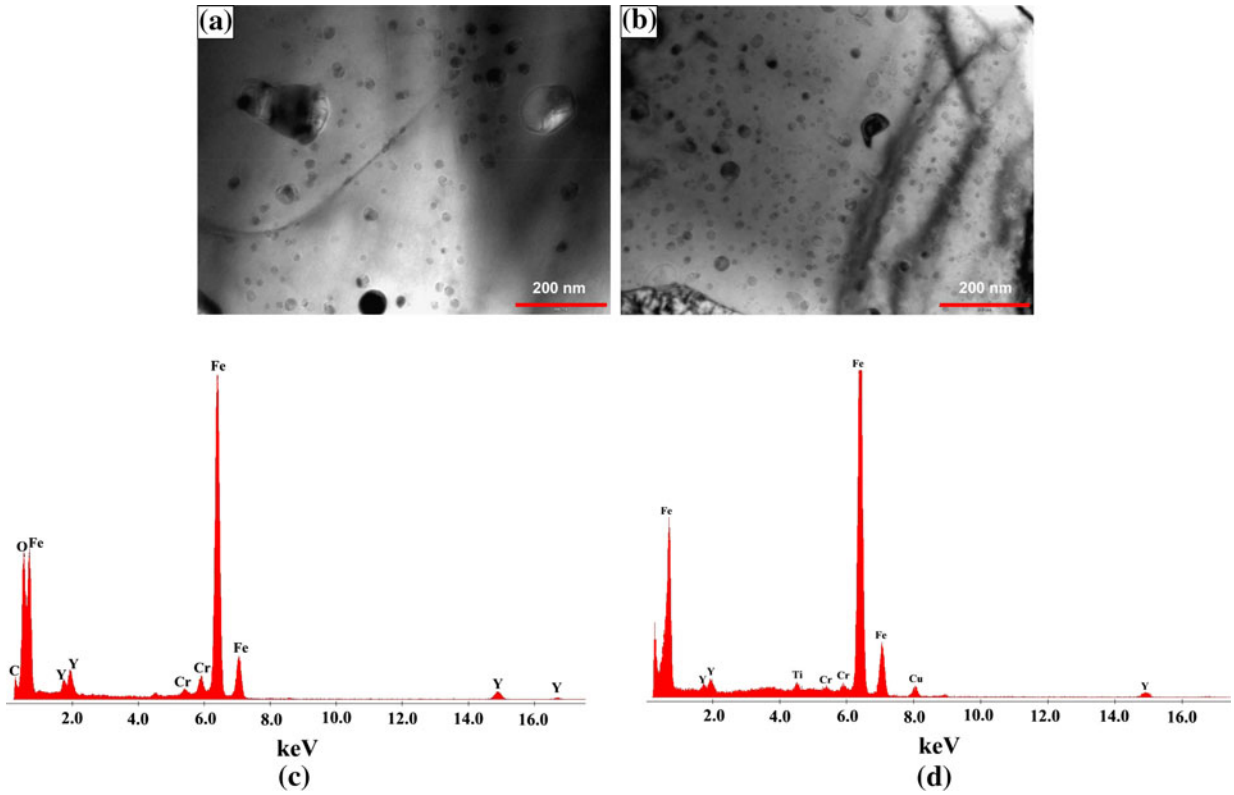

Fig. 4—TEM image of extruded rods showing oxide dispersoids: (*a*) Fe-Y_2O_3 and (*b*) Fe-Y_2O_3-Ti; EDS patterns of (*c*) Fe-Y_2O_3 and (*d*) Fe-Y_2O_3-Ti.

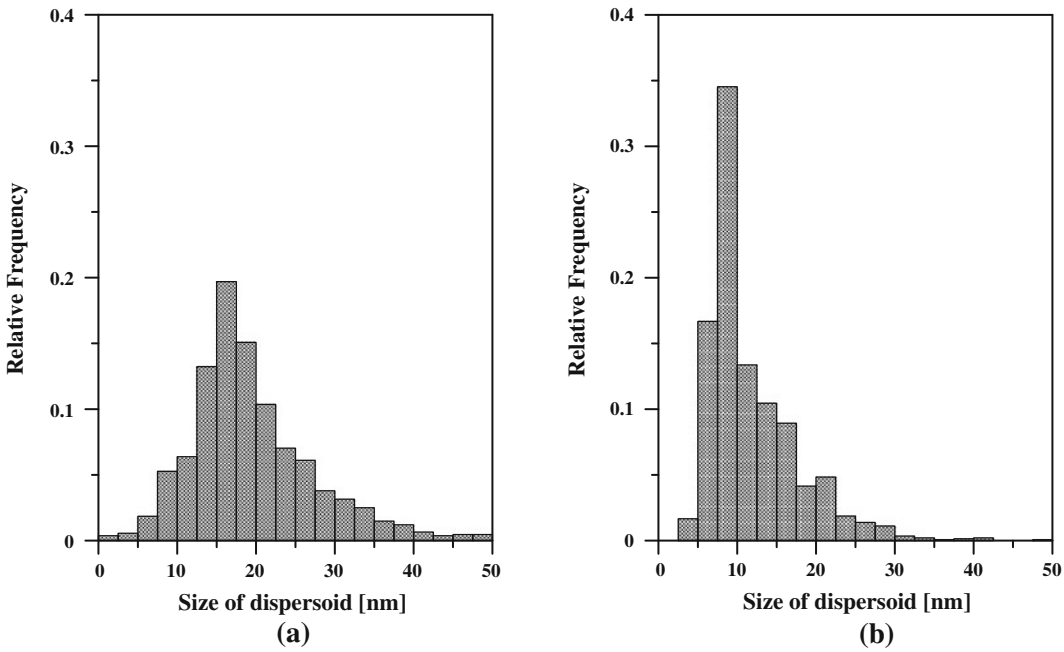

Fig. 5—Distribution of dispersoids in extruded and annealed rods of ODS iron: (*a*) Fe-Y_2O_3 and (*b*) Fe-Y_2O_3-Ti.

that the oxide complexes are of the type $Y_2Ti_2O_7$.[15] The presence of Cr was noticed in the EDS spectra of oxide particles, which was essentially due to the interference from the contamination of the matrix from the milling vial and media. The nature of the oxide particles and their sizes in ODS iron compositions are similar to those observed in more complex ferritic and martensitic chromium steels.[9,10,20–22] The inference is that the role

of variety and concentrations of the alloying elements in the ODS steel in dictating the composition, shape, and size of the oxide particles formed in Fe-based compositions is insignificant.

C. *Room Temperature Mechanical Properties*

The hardness data of extruded and annealed Fe, Fe-Y_2O_3, and Fe-Y_2O_3-Ti samples are shown in Figure 6. It is evident that the hardness of iron increases when fine Y_2O_3 dispersoids are present as in Fe-Y_2O_3. The hardness increase is more dramatic in Fe-Y_2O_3-Ti.

The room temperature tensile properties of Fe, Fe-Y_2O_3, and Fe-Y_2O_3-Ti are presented in Table III. The yield strength (YS) and ultimate tensile strength (UTS) increase in the order Fe, Fe-Y_2O_3, and Fe-Y_2O_3-Ti as in the case of hardness. However, it is to be noted that while addition of Y_2O_3 to iron increases the strength parameters only marginally, further addition of Ti increases the strength parameters dramatically. In contrast, the tensile elongation progressively decreases in the order Fe, Fe-Y_2O_3, and Fe-Y_2O_3-Ti. The higher hardness and YS of Fe-Y_2O_3-Ti when compared to Fe-Y_2O_3 and Fe is obviously caused, in addition to grain size refinement, by the reduced size and increased volume fraction of the $Y_2Ti_2O_7$ oxide particles as compared to the Y_2O_3 dispersoids in Fe-Y_2O_3 alloy.

It is now appropriate to attempt the quantification of various strengthening mechanisms in ODS iron. The well-known strengthening mechanisms like grain boundary strengthening (Hall–Petch) and dispersion hardening[23] are the relevant mechanisms in ODS Iron. The dispersion hardening can be the result of dislocations cutting the dispersoids or due to bowing of dislocations around the dispersoids (Orowan strengthening). Whether the dislocation cuts or bows around the dispersoid depend on the hardness, size of the dispersoids and the coherency of the dispersoid-matrix interface. Incoherent dispersoids cannot be cut by dislocations, and hence Orowan bowing is the only applicable mechanism. In the case of $Y_2Ti_2O_7$ dispersoids, recent work suggests that these dispersoids are semicoherent[24] and thus, in principle, dislocations can cut through these dispersoids. However, if the dispersoids are non-deformable due to its high hardness, then also Orowan bowing is the preferred mechanism. In the present case, the hardness of $Y_2Ti_2O_7$ (12.1 ± 0.1 GPa) is much higher than that of Y_2O_3 (6.9 to 9 GPa)[25] and thus cutting of $Y_2Ti_2O_7$ dispersoid is quite unlikely. In conclusion, the room temperature YS of ODS iron (σ_y) should be determined by matrix strength (σ_m), grain boundary strengthening due to Hall–Petch relationship ($\Delta\sigma_{H-P}$) and Orowan strengthening due to bowing of dislocation around dispersoids ($\Delta\sigma_{Or}$) as indicated below:

$$\sigma_y = \sigma_m + \Delta\sigma_{H-P} + \Delta\sigma_{Or} \quad [2]$$

The above parameters are described by the following equations.[19].

$$\Delta\sigma_{H-P} = K_{H-P} d_g^{-1/2} \quad [3]$$

$$\Delta\sigma_{Or} = A \cdot \left(\frac{Gb}{S}\right) \ln\left(\frac{d_p}{2b}\right) \quad [4]$$

$$\bar{d}_p = (2/3)^{1/2} d_p \quad [5]$$

$$S = \frac{d_p}{2}\left\{(2\pi/3f)^{1/2} - 2(2/3)^{1/2}\right\} \quad [6]$$

In the above equations, K_{H-P} is the Hall–Petch constant, d_g is the average grain size, A is a numerical constant, G and b are the matrix shear modulus and Burger's vector, d_p is the measured average dispersoid size, $\bar{d}_p$ is the mean diameter of spherical dispersoid in a random plane, f is the volume fraction of disperoids, and S is the inter-dispersoid spacing. Assuming $G = 82$ GPa, $b = 2.5 \times 10^{-10}$ m (values for iron), $A = 0.3$[19] and the values of other parameters as given in Table IV, the relative contributions of the various strengthening mechanism in the case of Fe, Fe-Y_2O_3, and Fe-Y_2O_3-Ti can be calculated. The results are presented in the form of bar charts in Figure 7(a). The experimentally obtained σ_y values are also included. From Figure 7(a), it is clear that the YS of Fe-Y_2O_3-Ti is predicted well by

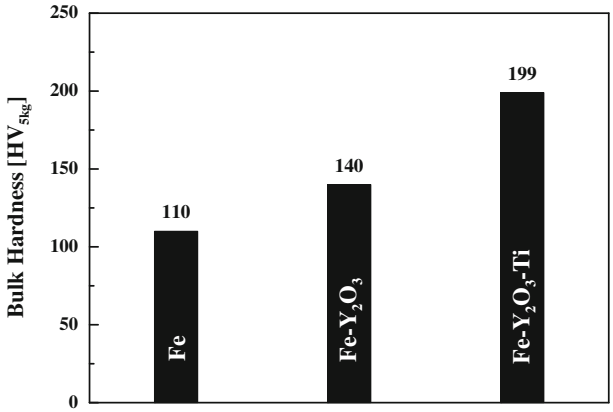

Fig. 6—Bulk hardness of extruded and annealed rods of Fe, Fe-Y_2O_3, and Fe-Y_2O_3-Ti.

Table III. Room Temperature Tensile Properties of Fe, Fe-Y_2O_3, and Fer-Y_2O_3-Ti

Material	YS (MPa)	UTS (MPa)	Elongation (Pct)	n
Fe	252	355	29	0.26
Fe-Y_2O_3	290	386	22	0.17
Fe-Y_2O_3-Ti	534	637	14	0.14

Table IV. Experimental Values of d_g, d_p, ND, and σ_y; Derived Values of $\bar{d}_p$, f, PAH and Literature Value of K_{H-P}

S. No.	Property	Fe	Fe-Y_2O_3	Fe-Y_2O_3-Ti	Source
1.	Average grain size (d_g) (μm)	14.0	11.0	8.0	Fig. 3
2.	Hall–Petch constant for yield strength (K_{H-P}) (GPa $nm^{1/2}$)	7.8	7.8	7.8	[19]
3.	Average dispersoid size (d_p) (nm)	—	20.5	12.0	Fig. 5
4.	Mean dia of spherical dispersoid in a random plane ($\bar{d}_p$)* (nm)	—	16.7	9.8	—
5.	Number density of dispersoids (ND) (no/m^3)	—	7×10^{21}	3.9×10^{22}	—
6.	Volume fraction of dispersoids (f)$^+$	—	0.00327	0.0104	—
7.	Room temperature yield strength (σ_y) (MPa)	252	290	534	Fig. 7(a)
8.	Projected area hardness (H)$^\#$ (MPa)	1172	1492	2120	Fig. 7(b)

*$\bar{d}_p = (2/3)^{1/2} d_p$.
†Calculated using average dispersoid size and number density.
#$H = (9.806/0.92)HV$.

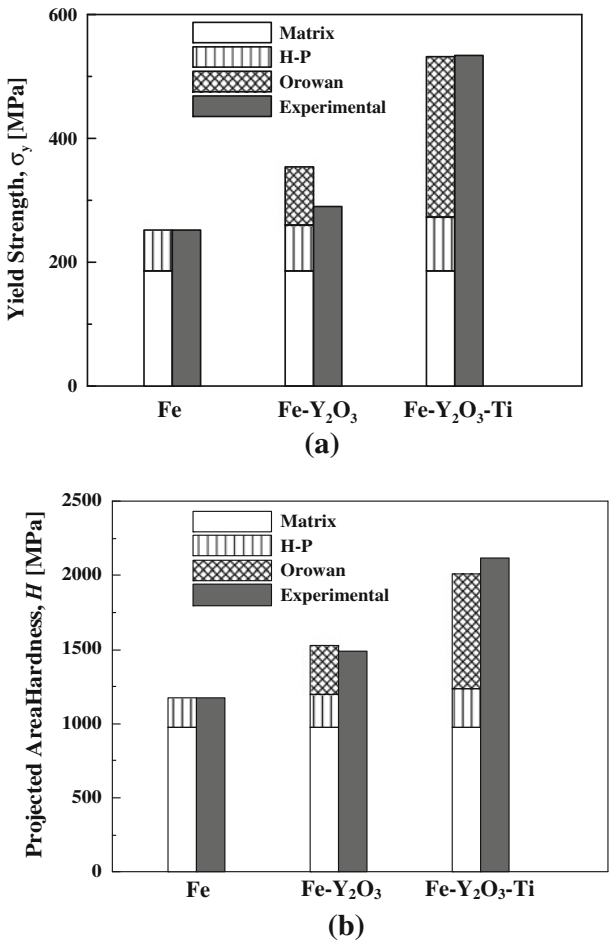

Fig. 7—Calculated strengthening values along with experimental values: (*a*) yield strength and (*b*) hardness.

the model, while the YS of Fe-Y_2O_3 predicted by the model is higher than the experimental value.

A similar exercise was carried out in respect of hardness of the Fe and ODS Fe using the values provided in Table IV. The results presented in Figure 7(b) indicate that the model predicts the hardness values very well in case of Fe, Fe-Y_2O_3, and Fe-Y_2O_3-Ti.

D. *Elevated Temperature Mechanical Properties*

The variation of UTS, YS and tensile elongation with increasing temperature is shown in Figures 8(a) through (c), respectively. The test results indicate the following:

(a) The UTS of Fe and ODS Fe increases with increasing temperature up to 573 K (300 °C). However beyond 573 K (300 °C), the UTS decreases substantially in all the 3 materials (Figure 8(a)).
(b) In the case of Fe and Fe-Y_2O_3, the YS decreases steadily with increasing temperature. In the case of Fe-Y_2O_3-Ti, the decrease in YS with temperature is marginal up to 573 K (300 °C) but substantial beyond 573 K (300 °C) (Figure 8(b)).
(c) At all test temperatures, Fe-Y_2O_3-Ti exhibits the highest strength parameters (YS and UTS) and Iron the lowest. However, at 723 K (450 °C), the strength of Fe-Y_2O_3-Ti is only marginally higher than Fe and Fe-Y_2O_3 indicating that the beneficial influence of fine dispersion of Y-Ti-O is on the decline (Figures 8(a) and (b)).
(d) The variation of tensile elongation with temperature (Figure 8(c)) points to a ductility minima at 423 K (150 °C) in the case of all the three materials. Beyond 423 K (150 °C), the elongation increases continuously with increasing temperature in all the three materials.
(e) The reasons for the dramatic decrease in YS beyond 573 K (300 °C) (Figure 8(b)) is not clear. It could be due to either grain or dispersoid coarsening or due to the increased influence of thermally activated deformation mechanisms. Further microstructural studies need to be carried out to clarify this aspect.

E. *Dynamic Strain Aging*

In pure bcc metals, reduction in strength and increase in ductility with increasing temperature should be

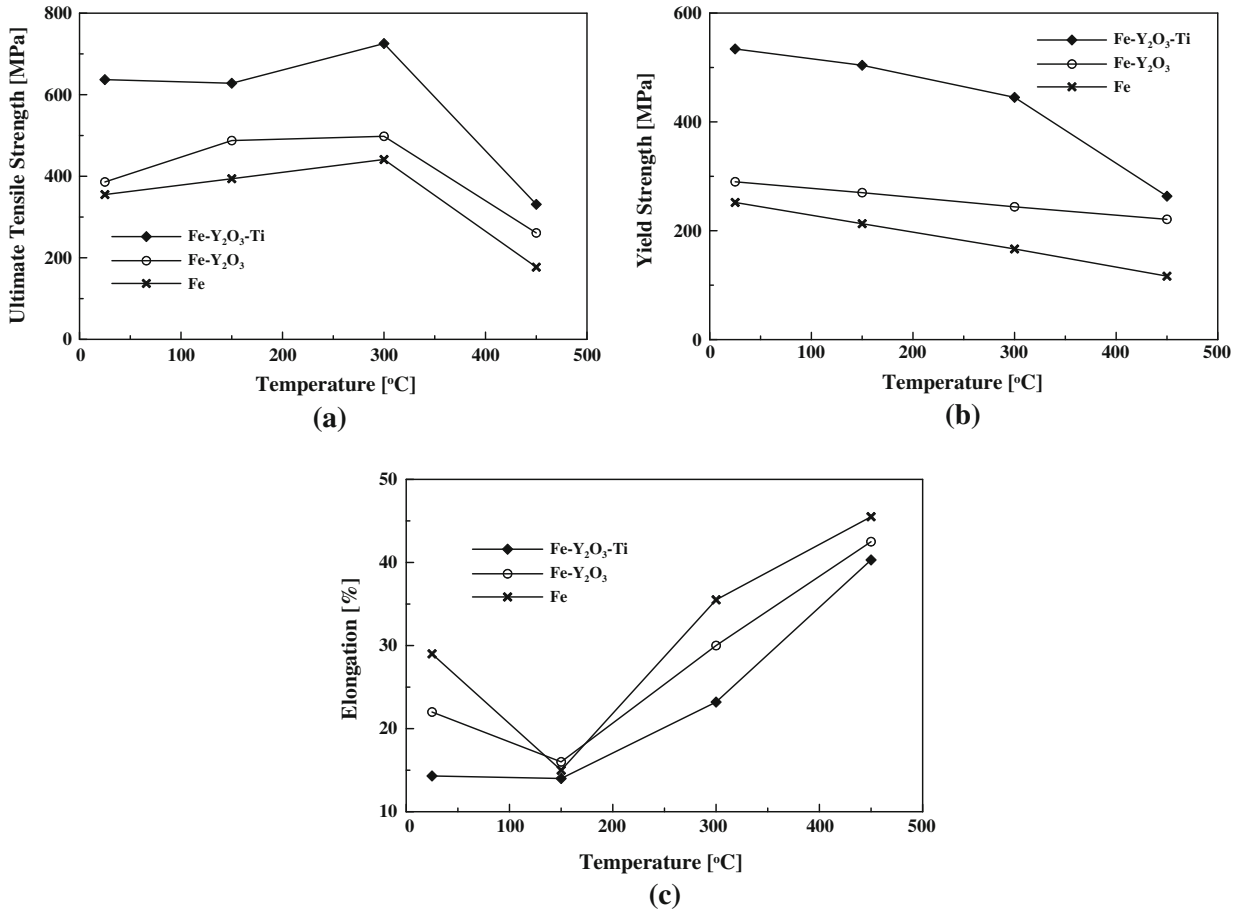

Fig. 8—Variation of tensile properties of Fe, Fe-Y_2O_3, and Fe-Y_2O_3-Ti with temperature: (*a*) UTS, (*b*) yield strength, and (*c*) elongation.

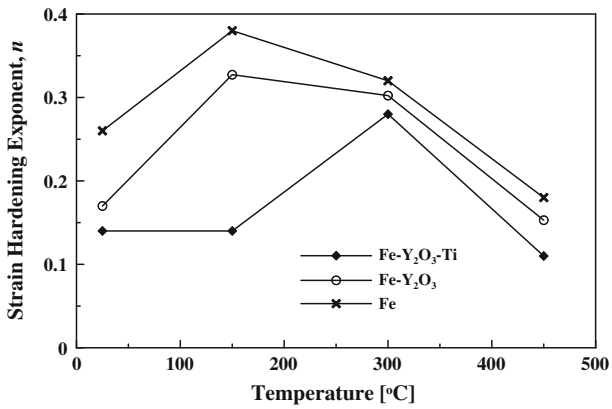

Fig. 9—Variation of strain hardening exponent with temperature.

expected. The observed increase in UTS and marginal decrease in YS in the temperature range of 423 K to 573 K (150 °C to 300 °C), when compared to room temperature strength, is attributable to dynamic strain aging (DSA). One typical feature of DSA is discontinuous yielding in tensile flow curves, which was noticed in the tests carried out at susceptible temperature range of 423 K to 573 K (150 °C to 300 °C). However, the dip in ductility in the DSA temperature range is considered to be due to the strain age embrittlement. To further confirm the operation of DSA, strain hardening exponent (n) was evaluated from the tensile test results for all the compositions at all test temperatures by fitting the true stress (σ) and true strain (ε) data in the constitutive equation, $\sigma = k\varepsilon^n$.The variation of n with temperature for Fe and ODS irons is shown in Figure 9. The data indicate that n reaches a maximum in the temperature range of 423 K to 573 K (150 °C to 300 °C) and that n is the highest in Fe and lowest in Fe-Y_2O_3-Ti. Both UTS and n are higher at 423 K to 573 K (150 °C to 300 °C) than those at room temperature which is confirmatory evidence of the occurrence of DSA and the temperature regime at which DSA occurs is in agreement with the reported data.[26] The solute atoms needed for DSA to pin mobile dislocations in ODS iron are nitrogen, carbon, and oxygen whose concentrations in the experimental materials are 180, 270, and 4700 ppm, respectively. It is well known that the addition of Ti to killed low carbon steels minimizes DSA by fixing N and C as nitrides, carbides, and carbo-nitrides. The occurrence of DSA in Fe and Fe-Y_2O_3 is justifiable because of the presence of excess oxygen and nitrogen picked up due to leakages during milling. However, the onset of DSA even in titanium- containing ODS Fe is surprising and can be attributed to the fact that the available titanium is completely tied up with oxygen to form Y-Ti-O complex oxides and TiO_2 leaving the solute atoms

(oxygen in excess of that tied up with Ti and nitrogen) free to move to and pin the dislocations in the DSA susceptible temperature range.

IV. CONCLUSIONS

Investigations on extruded and annealed rods of Fe, Ti, and Y_2O_3 powders to form Fe-Y_2O_3 and Fe-Y_2O_3-Ti revealed that:

- The oxide size decreases (12 nm) and number density increases ($3.9 \times 10^{22}/m^3$) in Fe-Y_2O_3-Ti when compared to dispersoid size of 20 nm and number density of $7 \times 10^{21}/m^3$ in Fe-Y_2O_3.
- Significant grain size reduction was observed in Fe-Y_2O_3-Ti due to the presence of finer and higher volume fraction of dispersoids. But the difference in grain size between Fe and Fe-Y_2O_3 is marginal due to less effective pinning of grain boundaries by the coarser and reduced number density of Y_2O_3 dispersoids.
- While hardness, YS, and UTS were higher, ductility and strain hardening exponent were lower in ODS irons when compared to iron at all test temperatures. However, at 723 K (450 °C), the difference in properties between iron and ODS irons is only marginal.
- The substantial increase in room temperature YS and hardness of Fe-Y_2O_3-Ti can be explained on the basis of higher contributions of grain boundary and dispersion strengths.
- The increasing UTS and strain hardening exponent up to 573 K (300 °C) and dip in ductility at 423 K (150 °C) are caused by dynamic strain aging.

ACKNOWLEDGMENTS

The authors thank Mr. G.V.R. Reddy for carrying out SEM examination. They are grateful to Dr. S.V. Kamat, Defence Metallurgical Research Laboratory, Hyderabad, for helpful suggestions during the course of the work.

REFERENCES

1. C. Zakine, C. Prioul, and D. Francois: *Mater. Sci. Eng. A*, 1996, vol. 219, pp. 102–08.
2. S. Ukai, T. Okuda, M. Fujiwara, T. Kobayashi, S. Mizuta, and H. Nakashima: *J. Nucl. Sc. Technol.*, 2002, vol. 39, pp. 872–79.
3. M.J. Alinger, G.R. Odette, and G.E. Lucas: *J. Nucl. Mater.*, 2002, vols. 307–311, pp. 484–89.
4. R.L. Klueh, P.J. Maziasz, I.S. Kim, L. Heatherly, D.T. Hoelzer, N. Hashimoto, E.A. Kenik, and K. Miyahara: *J. Nucl. Mater.*, 2002, vols. 307–311, pp. 773–77.
5. A. Alamo, V. Lambard, X. Averty, and M.H. Mathon: *J. Nucl. Mater.*, 2004, vols. 329–333, pp. 333–37.
6. D.S. Gelles: *J. Nucl. Mater.*, 1996, vols. 233–237, pp. 293–98.
7. S. Ukai and M. Fujiwara: *J. Nucl. Mater.*, 2002, vols. 307–311, pp. 749–57.
8. V. de Castro, T. Leguey, M.A. Monge, A. Muñoz, R. Pareja, D.R. Amador, J.M. Torralba, and M. Victoria: *J. Nucl. Mater.*, 2003, vol. 322, pp. 228–34.
9. M. Klimiankou, R. Lindau, and A. Moslang: *J. Cryst. Growth*, 2003, vol. 249, pp. 381–87.
10. A. Ramar, Z. Oksiuta, N. Baluc, and R. Schaublin: *Fusion Eng. Des.*, 2007, vol. 82, pp. 2543–49.
11. C. Cayron, E. Rath, I. Chu, and S. Launois: *J. Nucl. Mater.*, 2004, vol. 335, pp. 83–102.
12. M. Ratti, D. Leuvrey, M.H. Mathon, and Y. de Carlan: *J. Nucl. Mater.*, 2009, vols. 386–388, pp. 540–43.
13. M.K. Miller, D.T. Hoelzer, E.A. Kenik, and K.F. Russell: *J. Nucl. Mater.*, 2004, vols. 329–333, pp. 338–41.
14. M.J. Alinger, S.C. Glade, B.D. Wirth, G.R. Odette, T. Toyama, Y. Nagai, and M. Hasegawa: *Mater. Sci. Eng. A*, 2009, vol. 518, pp. 150–57.
15. S. Ohtsuka, S. Ukai, M. Fujiwara, T. Kaito, and T. Narita: *J. Nucl. Mater.*, 2004, vols. 329–333, pp. 372–76.
16. T. Okuda and M. Fujiwara: *J. Mater. Sci. Lett.*, 1995, vol. 14, pp. 1600–03.
17. K. Verhiest, A. Almazouzi, N. De Wispelaere, R. Petrov, and S. Claessens: *J. Nucl. Mater.*, 2009, vol. 385, pp. 308–11.
18. J.H. Schneibel and S. Shim: *Mater. Sci. Eng. A*, 2008, vol. 488, pp. 134–38.
19. R. Vijay, M. Nagini, M. Ramakrishna, J. Joardar, A.V. Reddy, and G. Sundararajan: *Metall. Mater. Trans. A*, 2013, vol. 44A, pp. 1611–20.
20. S.W. Kim, T. Shobu, S. Ohtsuka, T. Kaito, M. Inoue, and M. Ohnuma: *Mater. Trans.*, 2009, vol. 50, pp. 917–21.
21. S. Ohtsuka, S. Ukai, H. Sakasegawa, M. Fujiwara, T. kaito, and T. Narita: *J. Nucl. Mater.*, 2007, vols. 367–370, pp. 160–65.
22. A. Raman, N. Baluc, and R. Schaublin: *J. Nucl. Mater.*, 2009, vols. 386–388, pp. 515–19.
23. G.E. Dieter: *Mechanical Metallurgy*, 3rd ed., McGraw-Hill Book Co., London, 1988, pp. 212–19.
24. J. Ribis and Y. deCarlan: *Acta Mater.*, 2012, vol. 60, pp. 238–52.
25. L.F. He, J. Shirahata, T. Nakayama, T. Suzuki, H. Suematsu, I. Ihara, Y.W. Bao, T. Komatsu, and K. Niihara: *Scripta Mater.*, 2011, vol. 64, pp. 548–51.
26. M. Srinivas, S.V. Kamat, and P. Rama Rao: *Mater. Sci. Eng. A*, 2007, vol. 443, pp. 132–41.